Research Square

Preprints are preliminary reports that have not undergone peer review.
They should not be considered conclusive, used to inform clinical practice,
or referenced by the media as validated information.

Effect of fines content on reliquefaction resistance and consolidation–reconsolidation behavior of silty sand

Yeming Zhong
Central South University
Xueqian Ni
nixueqian@csu.edu.cn
Central South University
Sheng Zhang
Central South University
Zhao Zhang
Central South University
Feng Zhang
Tongji University
Feng Shan
Central South University

Research Article

Keywords: Fines content, Reliquefaction resistance, Reconsolidation, Stress-induced anisotropy, Silty sand

Posted Date: September 3rd, 2026

DOI: https://doi.org/10.21203/rs.3.rs-10721738/v1

License: This work is licensed under a Creative Commons Attribution 4.0 International License.
Read Full License

Additional Declarations: No competing interests reported.

Effect of fines content on reliquefaction resistance and consolidation–reconsolidation behavior of silty sand

Yeming Zhong[1] · Xueqian Ni[1*] · Sheng Zhang[1] · Zhao Zhang[2] · Feng Zhang[1,3] · Feng Shan[1]

[1] School of Civil Engineering, Central South University, Changsha 410075, China
[2] School of Geosciences and Info-Physics, Central South University, Changsha 410075, China
[3] College of Civil Engineering, Tongji University, Shanghai 200092, China
*Corresponding author (Xueqian Ni): nixueqian@csu.edu.cn

Abstract

According to traditional liquefaction theory, the process of densification after the first liquefaction makes the soil more resistant to future liquefaction events. However, this has been challenged by recent field observations that silty sand can reliquefy during subsequent aftershocks. Previous research has primarily focused on the consolidation and reliquefaction behavior of clean sand, leaving the mechanisms governing these processes in silty sand largely unexplored. In this study, a series of cyclic triaxial tests were conducted on eight sand mixtures with varying fines content (FC = 0% to 35%). The test results revealed that reliquefaction resistance increases with FC. It surpassed the first liquefaction resistance when $FC \geq 25\%$. For specimens prepared by the moist tamping method, inherent anisotropy initially decreased, then increased, and finally decreased again with increasing FC. Following liquefaction, the stress-induced anisotropy in the sand-like behavior region increased with FC, and continuously weakened while in the silt-like behavior region. An anisotropic coefficient ratio, R_{ac}, was proposed. It was found that reliquefaction resistance increases as R_{ac} decreases, and when $R_{ac} < 1$ and $FC \geq 25\%$, the reliquefaction resistance exceeds the first liquefaction resistance. Furthermore, meso-fabric observations were employed on specimens both before and after liquefaction.

Key words: Fines content, Reliquefaction resistance, Reconsolidation, Stress-induced anisotropy, Silty sand

1. Introduction

Traditional earthquake liquefaction theory posits that soil becomes more resistant to liquefaction due to densification through drainage after the first liquefaction. However, field investigations (Sims and Garvin 1995; Yasuda et al. 2012; Van Ballegooy et al. 2014; Lees et al. 2015) have revealed that previously liquefied sites can undergo liquefaction again, or even multiple times, a phenomenon known as reliquefaction. Notably, laboratory studies have consistently shown that the reliquefaction resistance of sand decreases significantly after the first liquefaction (Ha et al. 2011; Fardad Amini et al. 2021; Huang and Yuan 2026). This implies that even aftershocks with relatively low magnitude can significantly increase the potential of reliquefaction, thereby keeping the site continuously exposed to the risk of liquefaction. This apparent contradiction suggests that the evolution of liquefaction resistance cannot be fully explained by density changes during the consolidation phase alone. Instead, it

is likely closely related to intrinsic mechanisms induced by the mainshock, such as soil structure reorganization and alterations in particle arrangement (Yang and Huang 2023; Sukhumkitcharoen et al. 2024). Therefore, to ensure the long-term stability of foundation soil and substructure, a growing number of geotechnical engineers are investigating reliquefaction mechanism.

The key mechanisms governing large ground deformation were primarily governed by the shear behavior of soil during liquefaction and its subsequent reconsolidation process (Hussain and Sachan 2020). Current studies indicated that when shear strain exceeds a critical threshold (>7.5%), the resistance of soil to reliquefaction decreases substantially (Finn et al. 1970; Wahyudi et al. 2013; Fardad Amini and Wang 2024). This reduction in resistance was associated with the formation of columnar structures and unstable macropores following liquefaction. These structural features were more prone to instability under subsequent loading, further diminishing soil stability (Oda et al. 2001). During the first liquefaction, the sedimentary structure formed in the soil during the initial consolidation was completely destroyed, leading to the loss of its inherent anisotropy and the gradual development of a stress-induced anisotropic fabric (Ni et al. 2022a; Fardad Amini and Wang 2024). Ye et al. (2018) provided visual evidence through shaking table tests. The long axes of soil particles were observed to exhibit a distinctly vertical orientation after liquefaction by using digital imaging method. Furthermore, a greater prevalence of vertically oriented long axes was found to correlate with a higher susceptibility to liquefaction. As the degree of stress-induced anisotropy increases, the shear behavior of the soil in specific directions approximates that of a loose state, with a corresponding decrease in liquefaction resistance (Yamada et al. 2010). Notably, this anisotropic fabric is persistent and remains even after reconsolidation (Yamada et al. 2010; Ni et al. 2022b). During the subsequent reconsolidation phase, excess pore water pressure dissipates from the bottom upwards, leading to the formation of solidified sand layers (Wang et al. 2013; Fioravante et al. 2021). In this process, the total ground strain comprises two components: the axial strain developed during the first liquefaction and that developed during the reconsolidation phase (Liu et al. 2007). Research indicated that the maximum shear strain generated during the first liquefaction is one of the key factors controlling strain development during reconsolidation (Tsukamoto and Ishihara 2022). Furthermore, the soil permeability increases significantly after liquefaction, which accelerates excess pore water pressure dissipation and leads to greater settlement of the liquefied deposit during reconsolidation (Arulanandan and Sybico 1992). Consequently, most studies have focused on the structural evolution of post-liquefied soils and their underlying influence on cyclic response. However, research on soil consolidation behavior which before and after liquefaction remains limited, and the underlying mechanisms are not yet fully understood. Given the significant differences in soil structure before and after liquefaction, a thorough understanding of its consolidation behavior offers a new perspective for elucidating the

patterns of strain development and the mechanisms of reliquefaction.

While most laboratory investigations into the reliquefaction behavior have focused primarily on clean sand, field investigations showed that silty sand with varying *FC* can also exhibit significant liquefaction potential under seismic loading (Zhang et al. 2020; Manzanal et al. 2021; Minarelli et al. 2022). For instance, Cetin et al. (2025) documented liquefaction in a soil containing 27.2% fines during the 2023 Turkey earthquake. Koester (1994), through a series of triaxial tests, demonstrated that under constant void ratio conditions, liquefaction resistance first decreases and then increases with increasing *FC*. Furthermore, the presence of fines significantly alters the physical properties of the soil (Cheng et al. 2019; Monkul and Tütüncü 2024). Mekkiyah and Al-Khazragie (2015) noted that an increase in *FC* raises both the compression index and the plasticity index of the soil. Lipiński et al. (2017) further found that increasing *FC* not only increases the volumetric strain at the end of consolidation but also significantly prolongs the time required to complete consolidation. Based on these findings, it is evident that *FC* significantly influences both the mechanical properties of silty sand and their liquefaction behavior. However, in-situ soil widely consists of sand-silt mixtures with varying *FC*, whose mechanical behavior lies between that of clean sand and pure silts (Seed et al. 1983; Holzer et al. 2010; Shivaprakash and Dinesh 2017). Therefore, how *FC* influences the consolidation/reconsolidation process and reliquefaction behavior of these transitional soils remains to be further elucidated.

This study conducted a series of cyclic triaxial tests on Fujian sand with varying *FC* to investigate the effects on reliquefaction behavior and strain development characteristics during both consolidation and reconsolidation. Firstly, the influence of *FC* on liquefaction behavior of clean sand was examined, and the evolution of stress-induced anisotropy was investigated in relation to the strain development characteristics during consolidation/reconsolidation. Then, the relationship between reliquefaction resistance and strain characteristics during consolidation/reconsolidation was analyzed detailly for soil with various *FC*. A new anisotropy coefficient ratio was proposed to characterize the relationship between the reliquefaction resistance and the first liquefaction resistance in silty sand. Additionally, scanning electron microscopy (SEM) was employed to discuss and analyze the changes in the fabric of silty sand from a mesoscale perspective.

2. Experimental material and method

2.1 Experimental materials and apparatus

In this study, silty sand was prepared by mixing Fujian sand with marine-deposited silt. The grain size distribution curves of the two materials are shown in Fig. 1. Fujian sand is a naturally occurring, clean, yellowish,

sub-angular quartz sand. The marine-deposited silt is generally loose and friable, with a smooth texture and a yellowish-brown color, exhibiting no noticeable granularity. Table 1 presents the basic properties of the two base soils. Additionally, eight types of silty sand with varying *FC*, ranging from 0% to 35%, were prepared. The maximum and minimum void ratios for each *FC* were determined following ASTM D4253 and ASTM D4254, respectively. The detailed parameters are provided in Table 2.

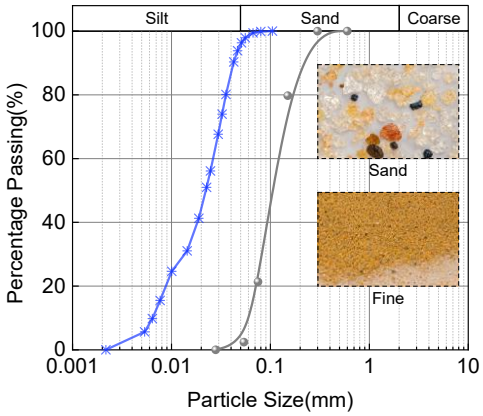


Fig. 1 The grain size distribution of Fujian sand and silt

Table 1 The basic properties of base soil

Soil type	G_s	C_c	C_u	D_{50}	I_P
Fujian sand	2.65	1.13	1.50	0.17	
Marine silt	2.68	1.07	3.99	0.02	20.30

The experimental apparatus used in this study was a self-developed pneumatic triaxial testing system, as shown in Fig. 2. The system comprises four main components: a triaxial pressure chamber, a pressure control system, a servo control system, and a data acquisition system. It is capable of offering stress-controlled or strain-controlled loading conditions. During testing, the system monitors the axial displacement, axial load, pore water pressure, and volume change of the specimen in real time. Axial load and displacement are applied through a pneumatic loading system at the top of the cell and are recorded by an integrated high-precision displacement transducer. It can apply sinusoidal cyclic loading with frequencies ranging from 0.01 Hz to 10.00Hz, while the axial displacements are measured using a displacement transducer with a range of ± 20.00 mm. Furthermore, by coordinating the pressure control panel and the water and pressure unit, the confining pressure in the triaxial chamber and the back pressure within the specimen can be independently regulated. This allows for precise control of the specimen's effective stress state under various conditions. To measure the volume change of saturated specimens, the system is also equipped with a high-precision volume gauge transducer with a range of 25.00 ml and a measurement accuracy of 0.01 ml.

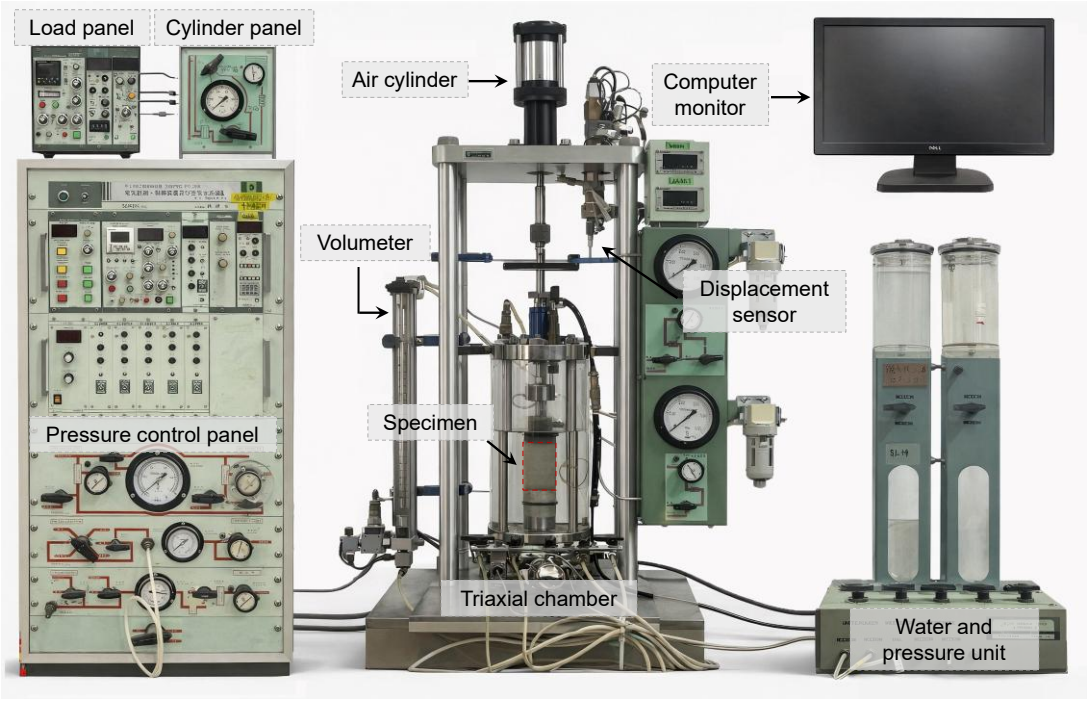


Fig. 2 Schematic diagram of the test apparatus

2.2 Sample preparation and test procedures

To prevent particle segregation caused by air or water flow and to effectively control the overall density of the specimens, the silty sand was prepared using the moist tamping method. During preparation, the fines were first thoroughly mixed with the Fujian sand. Then, 5% de-aired water was added, and the mixture was blended until uniform. The sand-fines mixture was then placed into a cylindrical mold and compacted in five layers of equal height to produce specimens with a diameter of 50 mm and a height of 100 mm. After preparation, the specimen was connected to the loading system, and a confining pressure of 30 kPa was applied to maintain its stability. To ensure full saturation, the specimen was first flushed with de-aired water and percolated with CO_2. A back pressure of 200 kPa was then applied to dissolve the residual carbon dioxide. Saturation was considered complete when a *Skempton B* value greater than 0.95 was achieved.

All loading stages were conducted under undrained conditions. The soil specimens were then isotropically consolidated under an effective mean stress of 100 kPa. Consolidation was considered complete when no further increase in excess pore water pressure was observed within five minutes of closing the top and bottom drainage valves. After consolidation, a cyclic stress-controlled load was applied to the specimen in the form of a sinusoidal wave at a frequency of 0.01 Hz. To facilitate comparison with existing studies, a cyclic stress ratio (*CSR*) of 0.20 was selected, corresponding to a cyclic stress amplitude of 40 kPa. Furthermore, to extend the investigation of the influence of *FC*, additional tests were conducted at a *CSR* of 0.10. During cyclic loading, liquefaction was defined

as the point at which the double amplitude axial strain reached 5%. The number of cycles required to reach this criterion was recorded as N_c. Following liquefaction, the drainage valves were opened, and the specimen was allowed to reconsolidate under a confining pressure of 100 kPa. After reconsolidation was complete, the same specimen was subjected to an identical cyclic loading protocol to simulate the response of a site subjected to two consecutive seismic events. Table 2 shows the test conditions, where volumetric and axial strain refer to the respective values during the consolidation stage before liquefaction.

Table 2 Triaxial test conditions

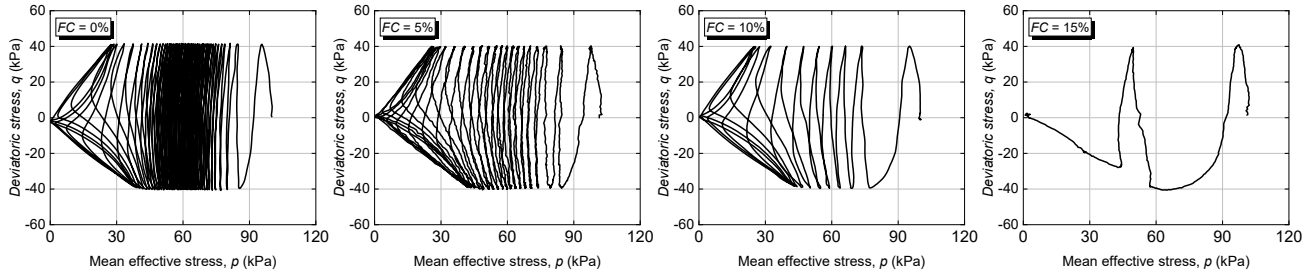
FC (%)	Liquefaction event	e_{max}	e_{min}	*CSR*	Volumetric strain, ε_v (%)	Axial strain, ε_a (%)	Number to liquefaction, N_c
0	1st	1.008	0.626	0.20	0.344	0.162	50
5		1.029	0.560		0.364	0.171	22
10		1.084	0.494		0.477	0.173	11
15		1.123	0.453		0.712	0.194	2
20		1.143	0.407		1.273	0.240	2
20	1st	1.143	0.407	0.10	1.322	0.226	16
25		1.159	0.385		3.057	0.346	5
30		1.171	0.392		3.294	0.486	12
35		1.180	0.426		3.553	0.543	14
0	2nd	1.008	0.626	0.20	1.285	0.121	4
5		1.029	0.560		1.490	0.245	3
10		1.084	0.494		1.734	0.257	2
15		1.123	0.453		2.405	0.341	1
20		1.143	0.407		3.740	0.503	1
20	2nd	1.143	0.407	0.10	4.158	0.422	6
25		1.159	0.385		4.802	0.791	5
30		1.171	0.392		5.188	1.336	19
35		1.180	0.426		5.454	1.538	33

3. Test results

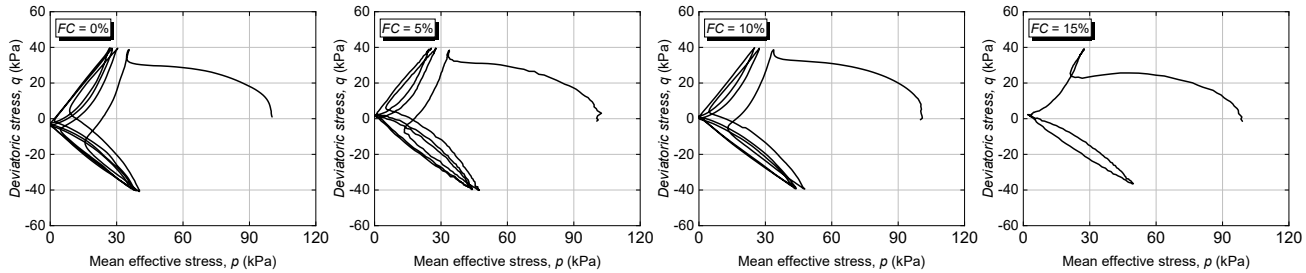
3.1 Influence of *FC* on liquefaction response

In this section, the results of eight undrained cyclic triaxial tests were presented to elucidate the influence of *FC* on liquefaction response mechanisms. Figure 3 illustrates the first liquefaction and reliquefaction responses for specimens with *FC* ranging from 0% to 15% under a *CSR* of 0.20. As shown in Fig. 3a, the specimens with *FC* of 0%, 5%, and 10% failed in a typical cyclic liquefaction mode. The effective stress decreased progressively with an increasing number of loading cycles. As the mean effective stress approached zero, the stress path exhibited repeated

dilation and contraction on both the compression and extension sides, forming a characteristic of butterfly shape. For the specimens with *FC* of 0%, 5%, and 10%, the number of cycles required to trigger liquefaction was 50, 22, and 11, respectively. In contrast, the specimen with *FC* of 15% failed in a typical flow liquefaction mode. This mode was characterized by a rapid increase in both excess pore water pressure and axial strain as the stress approached zero, with liquefaction occurring after only 2 cycles. Overall, during the first liquefaction event, the liquefaction resistance decreased as the *FC* increased from 0% to 15%. However, the evolution of mean effective stress for reliquefied specimens was remarkably similar in Fig. 3b, all showing a direct entry into cyclic liquefaction phase within a single cycle. This phase was marked by a rapid accumulation of axial strain until liquefaction occurred. Compared to the first liquefaction resistance shown in Fig. 3a, the number of cycles to reliquefaction for the different *FC* was 4, 3, 2, and 1, respectively.



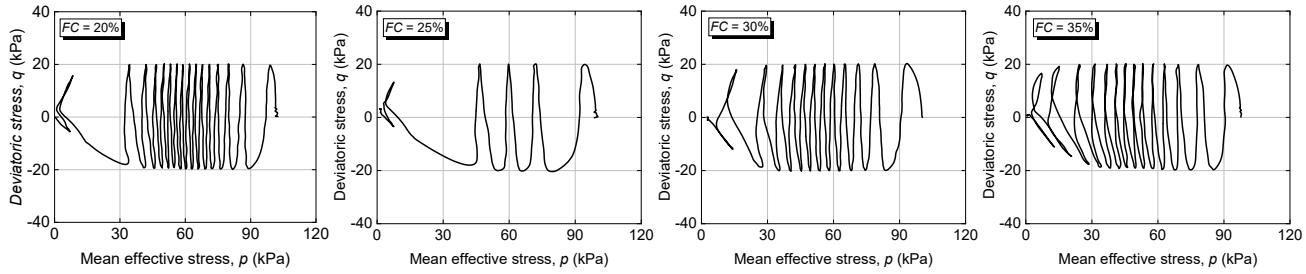
(a) First liquefaction



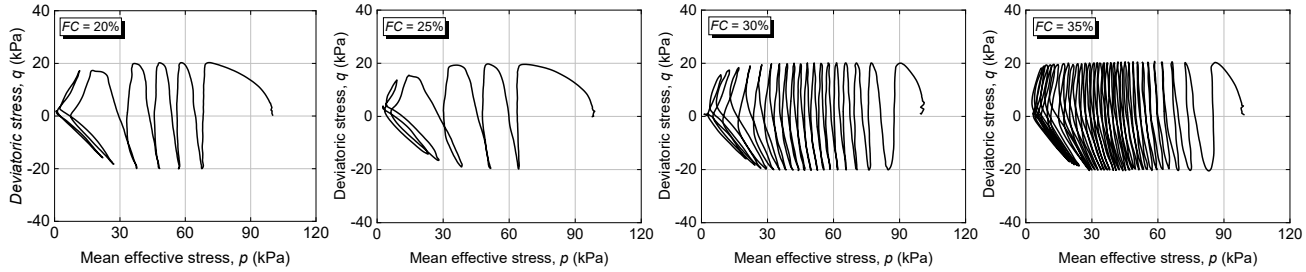
(b) Reliquefaction

Fig. 3 Liquefaction and reliquefaction responses with varying *FC* from 0-15% (*CSR*=0.20)

It is noteworthy that when the *FC* was increased to 20%, the specimen failed after only one cycle of loading. This behavior was also observed for *FC* values of 25% and 30%. Therefore, to further investigate the influence of *FC* on the liquefaction resistance of silty sand, four additional tests were conducted for *FC* values ranging from 20% to 35% at a *CSR* of 0.10, with the results shown in Fig. 4. As shown in Fig. 4a, the specimens required 16, 5, 12, and 14 cycles to failure, respectively. As *FC* increased from 20% to 35%, the first liquefaction resistance initially decreased and then increased. However, the stress paths during reliquefaction shown in Fig. 4b differed from those previously observed for the 0%-15% *FC* specimens. Before entering the cyclic liquefaction phase, a variable number of cycles was required for the accumulation of excess pore water pressure, with liquefaction finally occurring at 6, 5, 19, and 33 cycles.



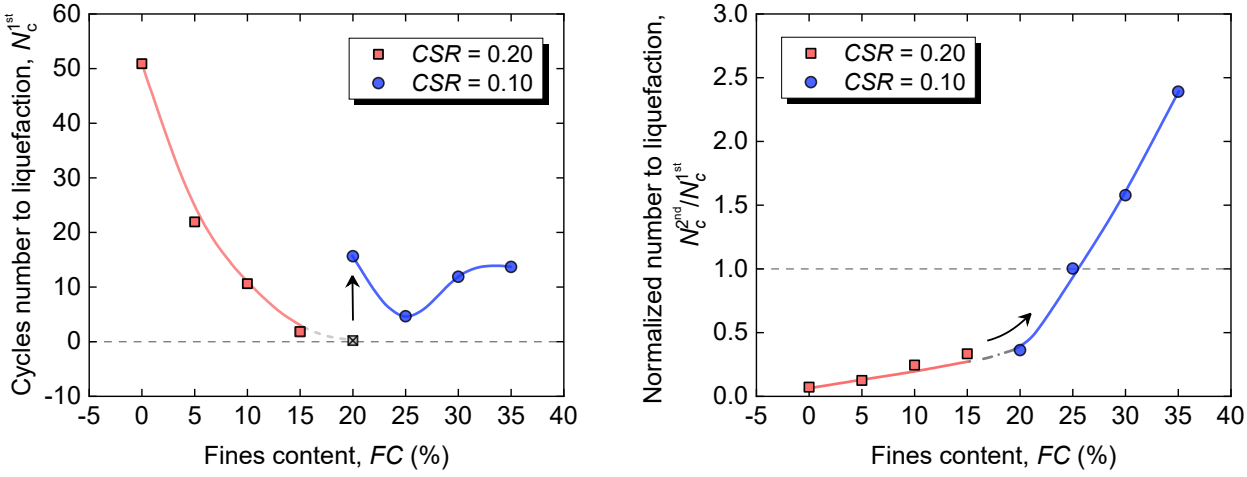
(a) First liquefaction



(b) Reliquefaction

Fig. 4 Liquefaction and reliquefaction responses with varying *FC* from 20-35% (*CSR*=0.10)

As shown in Fig. 5a, the first liquefaction resistance initially decreases and then increases with *FC*, with a notable increase observed for *FC* exceeding 25%. This is the threshold value of 29% for the silty sand that exhibits the minimum liquefaction resistance (Zhang et al. 2025). To compare the resistance during the first and second liquefaction events, the relative value of reliquefaction resistance, which is quantified by the ratio of cycle number required for reliquefaction to that for the first liquefaction, denoted as N_c^{2nd}/N_c^{1st}, is defined in this study. Figure 5b further demonstrates that under both 0.10 and 0.20 *CSR* conditions, the relative reliquefaction resistance increases significantly with *FC*, with a more pronounced increase observed at *CSR* = 0.10. Furthermore, when *FC* ≥ 25%, the reliquefaction resistance not only becomes higher than the first liquefaction resistance for the first time but also continues to increase with further increases in *FC*.



(a) Number of cycles to first liquefaction (b) Normalized number of cycles to liquefaction

Fig. 5 Relationship between *FC* and liquefaction resistance

3.2 Influence of *FC* on strain development during consolidation/reconsolidation

The consolidation behavior of the soil varies significantly with changes in *FC*. Figure 6 illustrates the development of volumetric strain during both the initial consolidation and reconsolidation for silty sand. As shown in Fig. 6a, during the initial consolidation, the volumetric strain of all specimens increased continuously with increasing *FC*. For specimens with lower *FC* (0%-15%), the volumetric strains developed slowly under the same confining pressure. However, when *FC* reached 20%, a clear increase in volumetric strain was observed. This indicates that the overall compressibility of the soil increases with increasing *FC*. A similar trend in volumetric strain development was observed during the reconsolidation phase, as shown in Fig. 6b. However, compared to the initial consolidation, the volumetric strain of the silty sand was consistently higher during reconsolidation. This increase was particularly pronounced for *FC* value exceeding 20%.

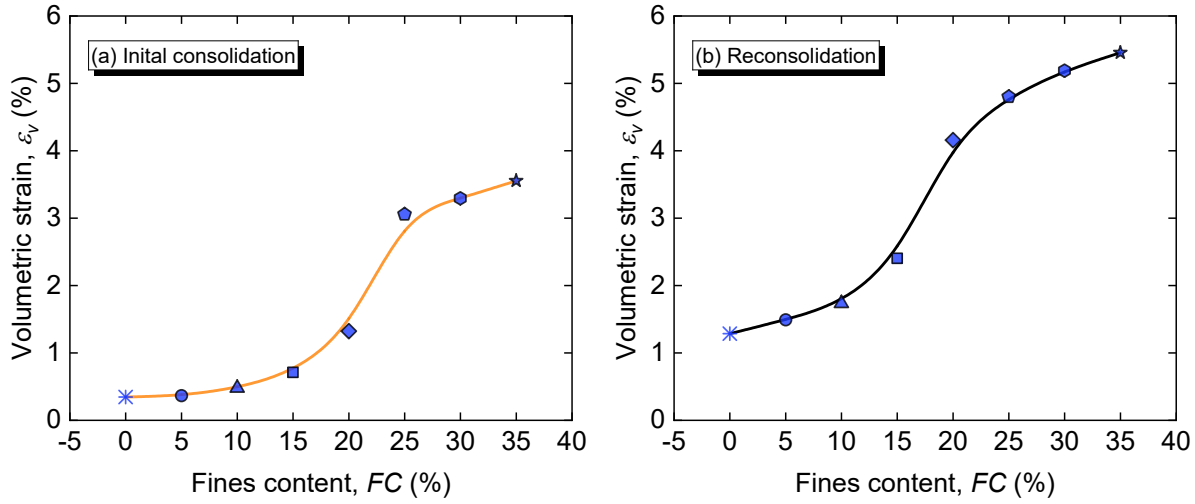


Fig. 6 Strain development characteristics of silty sand during consolidation/reconsolidation

Figure 7 presents the relationship between axial strain and volumetric strain observed during the consolidation/reconsolidation process. The black dash-dotted line represents the isotropic consolidation line (ICL). This line reflects the theoretical relationship between axial strain and volumetric strain during ideal isotropic consolidation, specifically that $\varepsilon_v=3\varepsilon_a$ (Ishihara and Okada 1978). During the initial consolidation (prior to the first liquefaction), the strain development of all specimens exhibited a distinct two-stage behavior. Specifically, for *FC* between 0% and 15%, the relationship between axial and volumetric strain closely followed the ICL. As *FC* increased to 20%, the development of axial and volumetric strain maintained a similar consolidation trend, although the strain paths gradually diverged from the ICL. For *FC* exceeding 20%, the development of axial strain accelerated significantly relative to volumetric strain. The corresponding paths initially deviated from the previous linear trend but then converged towards the ICL. In contrast, the strain behavior during reconsolidation exhibited a three-stage pattern, with all strain paths located above the ICL. Clean sand (*FC*=0% and 5%) exhibited a characteristic of low axial strain but high volumetric strain during reconsolidation, a pattern that differed from that of silty sand. For specimens with *FC* between 5% and 15%, the strain development during reconsolidation followed a relatively consistent trend, gradually deviating further from the ICL as *FC* increased. However, when *FC* exceeded 15%, the paths during reconsolidation showed a tendency to converge back towards the ICL, a behavior similar to that observed during initial consolidation.

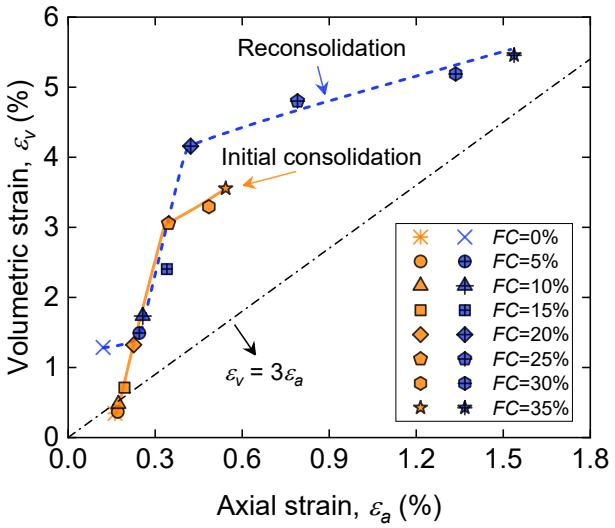


Fig. 7 Relationship between axial and volumetric strain during consolidation/reconsolidation

As suggested by Ishihara and Okada (1978), the ratio of volumetric strain to axial strain can be used to quantify the current anisotropy level of the soil. A value of 3.0 corresponds to an isotropically consolidated state, while the ratio greater than 3.0 implies higher compressibility in the horizontal direction than that in the vertical direction. Hence, Figure 8 illustrates the evolution of macroscopic anisotropy for different *FC* values before and after liquefaction. Based on the framework of Thevanayagam et al. (2001), the soil behavior transitioned from that of a clean sand, to a sand-like, and finally to a silt-like behavior as *FC* increases. For silty sand, the ratio exhibits a similar trend during the initial consolidation and reconsolidation. Under sand-like region, the ratio increased as rising FC, whereas it declines continuously under silt-like region. Specifically, the inherent anisotropy of specimens prepared by moist tamping initially decreased and then gradually increased as *FC* increased in the sand-like behavior region, while the horizontal compressibility of the soil continuously increased. For *FC* exceeding 15%, the specimens exhibited a high level of anisotropy, reaching a maximum at *FC* = 25%. In the silt-like behavior region, the inherent anisotropy of the soil decreased slightly. Upon entering the reconsolidation phase, the liquefaction event substantially rewrote the inherent anisotropy. As excess pore water pressure dissipated and residual strains developed, stress-induced anisotropy was generated while particles tending toward a vertical orientation (Ye et al. 2018; Ni et al. 2022a). As can be seen in the figure, the stress-induced anisotropy of clean sand was consistently higher than that of silty sand, suggesting that the presence of fines weakened expression of stress-induced anisotropy. However, as *FC* increased within this region, the anisotropy of silty sand also increased, reaching a maximum at *FC* = 20%. Beyond this point, as *FC* increased further and the soil enters the silt-like behavior region (starting from approximately 25% *FC*), the level of anisotropy decreased steadily, eventually approaching the ICL. A more detailed discussion of the underlying mechanisms was provided in Section 3.3.

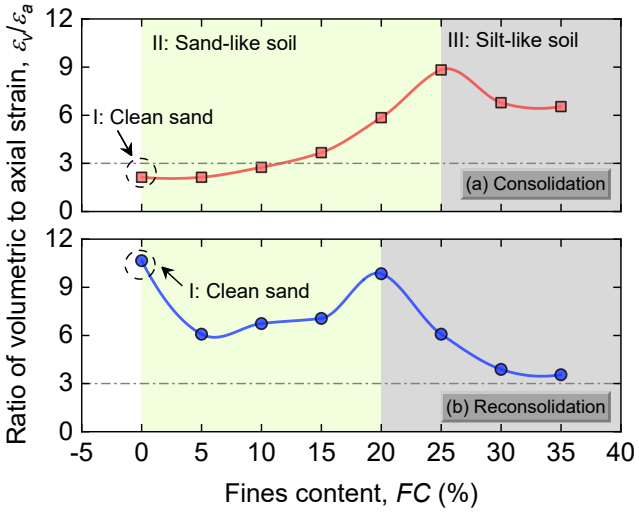


Fig. 8 Relationship between *FC* and anisotropy before and after liquefaction

To quantify the influence of anisotropy evolution on the reliquefaction resistance of silty sand, this study proposes an anisotropic coefficient ratio, denoted as R_{ac}. This ratio is defined as the quotient of the volumetric-to-axial strain ratio during reconsolidation divided by the corresponding ratio during the initial consolidation:

$$R_{ac} = \frac{(\varepsilon_v/\varepsilon_a)_{Re}}{(\varepsilon_v/\varepsilon_a)_{ini}} \quad (1)$$

Figure 9 illustrates the relationship among the R_{ac}, reliquefaction resistance, and *FC*. The left black ordinate represents the reliquefaction resistance, while the right purple ordinate indicates the *FC*. As can be seen from the figure, R_{ac} decreased consistently with increasing *FC*, and its trend shown a strong consistency with that of the reliquefaction resistance. Notably, the reliquefaction resistance was consistently lower than the first liquefaction resistance when R_{ac} was greater than 1.0, and this occurred for *FC* less than 25%. Conversely, when R_{ac} was less than 1.0 (indicated by the red region), the reliquefaction resistance exceeded the first liquefaction resistance, corresponding to *FC* greater than 25%. This demonstrates a clear relationship among R_{ac}, *FC*, and reliquefaction resistance, suggesting that R_{ac} could serve as an effective indicator for evaluating potential in reliquefaction. In practice, for soil with a R_{ac} of less than 1.0, it may possess greater resistance to subsequent dynamic loading than it did during the first liquefaction. This provides valuable insights for engineering in seismically active regions or for projects where the risk of multiple liquefaction events must be considered. A combined assessment of *FC* and R_{ac} could inform differentiated mitigation strategies for various strata at reliquefaction sites. For instance, in zones characterized by low R_{ac} and high *FC*, the stress-induced anisotropy of the reliquefied site may no longer be the dominant factor controlling reliquefaction resistance.

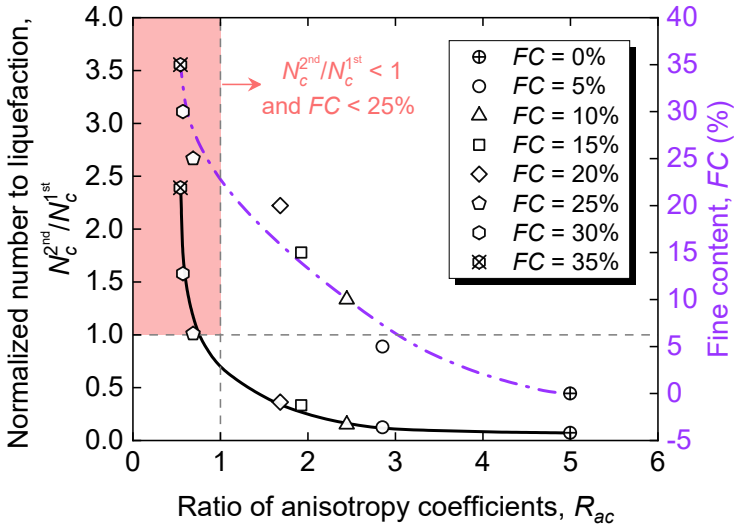


Fig. 9 Relationship among the R_{ac}, FC, and reliquefaction resistance

3.3 Influence of liquefaction on the meso-fabric of silty sand

According to Heng et al. (2001), the liquefaction resistance of silty sand would decrease gradually with the increasing of FC, which was attributed to the lubricating effect of fine particles within the soil skeleton. This phenomenon was also observed in this study. However, for silty soil with larger FC, liquefaction resistance tends to increase, the fabric evolution for which has not been clarified now. Therefore, to provide a more direct explanation for the increase in liquefaction resistance observed in silty sand with large FC (20%~35%), scanning electron microscopy (SEM) was employed to examine the longitudinal sections of specimens with FC ranging from 20% to 35%. The meso-fabrics of the specimens before and after liquefaction are shown in Figs. 10 and 11, respectively. It should be noted that the state before liquefaction refers to the specimens after preparation, whereas the state after liquefaction refers to the specimens that had undergone the first liquefaction and subsequent reconsolidation. As shown in Fig. 10a, under sand-like behavior conditions (FC = 20%), the fabric was primarily composed of a sand skeleton, with fines distributed within the pores. These fine particles acted as fillers and developed three contact modes with the sand particles: point-to-point, diffuse and surface contact, which were marked in yellow, blue and green, respectively. When FC increased ($\geqslant$ 25%), the fine particles gradually replaced sand particles and became a major constituent of the soil skeleton. As shown in Fig. 10c, point contact between fine and sand particles was scarcely observed at this stage. Concurrently, the diffuse and surface contact areas continued to expand, increasing the coverage area of the sand. This process led to a gradual reduction in direct sand particles contacts. Consequently, the sand was gradually encapsulated by the aggregates formed by the silt, as illustrated in Fig. 10d. This transition in

contact mode led to a more uniform pore distribution within the soil. This meso-fabric evolution provided a reasonable explanation for the observed increase in liquefaction resistance (Bao et al. 2024).

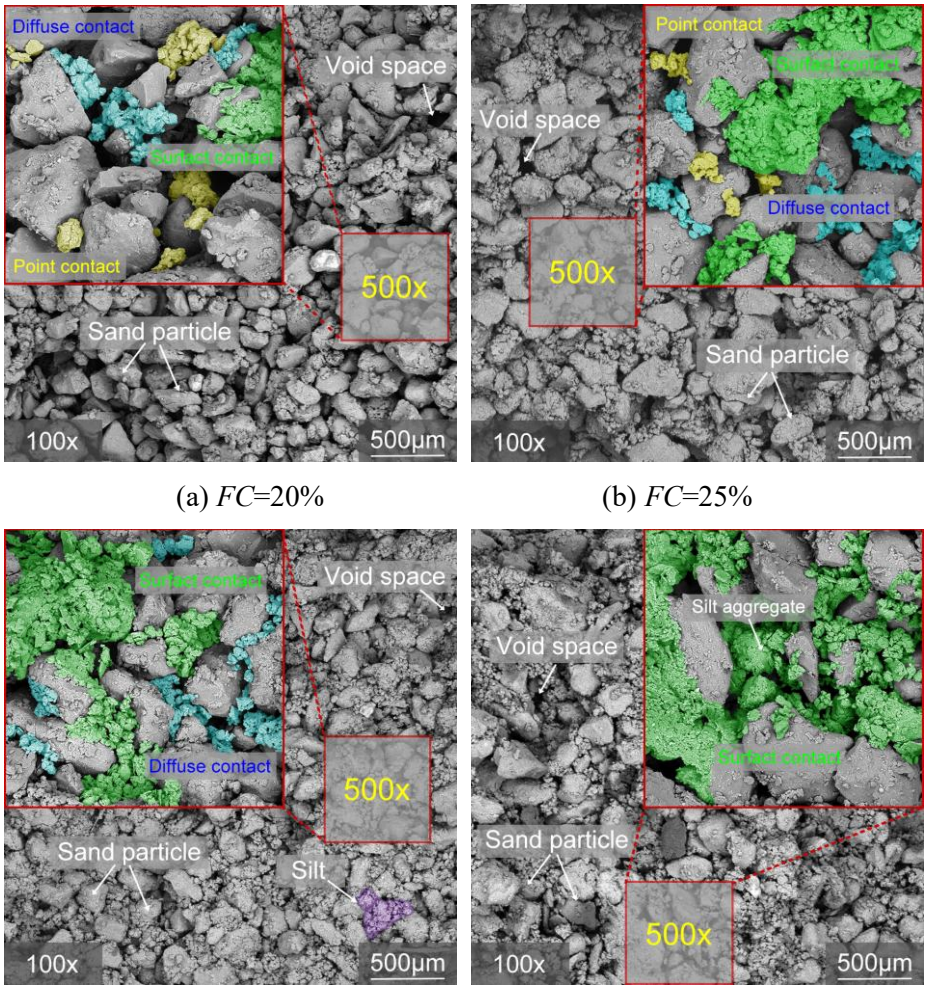
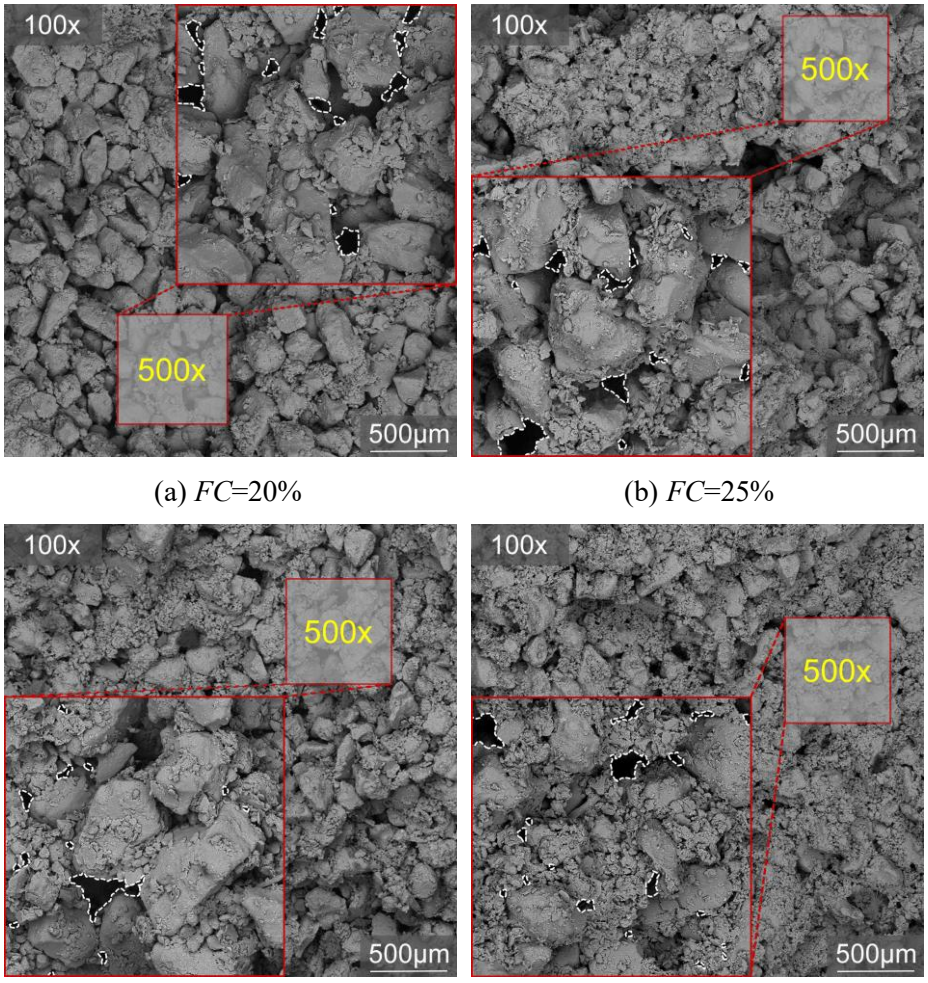


Fig. 10 Meso-fabric of soil specimen prepared by the moist tamping method (at 100× magnification)

The meso-fabric of a specimen after the first liquefaction is shown in Fig. 11. After liquefaction, the dissipation of excess pore water pressure generated drainage pathways, as indicated by the white dashed line. These newly formed pathways competed with the fine particles for limited space within the pore network. On one hand, the emergence of these new pathways altered the original pore structure. On the other hand, the overall densification of the soil promotes the transformation of large pores into smaller ones. During this process, the contact mode between sand and fine particles evolved from point or diffuse contacts to more intimate surface contacts. Once this coating fabric was fully developed, the sand particles become effectively isolated by the fines. As the continuity of the sand skeleton was disrupted, fabric anisotropy can no longer be effectively transmitted through the granular framework. Consequently, the macroscopic expression of stress-induced anisotropy was weakened, even though the granular reorientation still occurred after liquefaction. This meso-fabric evolution mechanism further explains why the specimen with FC = 20% exhibited strain development characteristics similar to silt-like soils during the reconsolidation process, while simultaneously the reliquefaction resistance of the silty sand increased with rising FC.



(a) *FC*=20% (b) *FC*=25%

(c) *FC*=30% (d) *FC*=35%

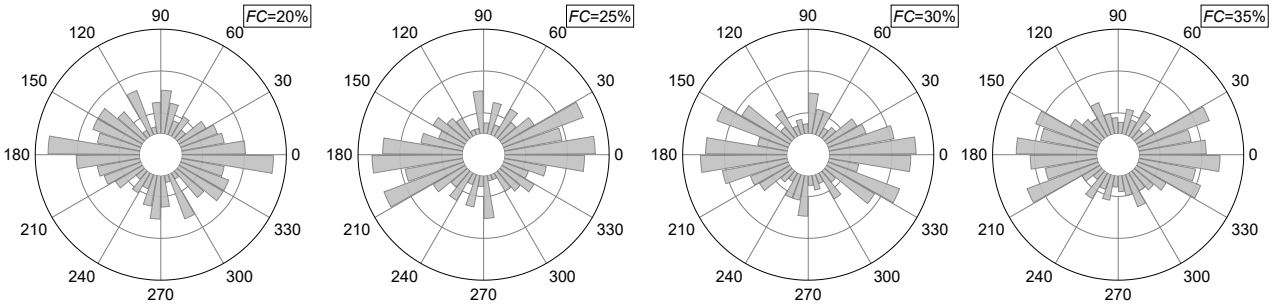
Fig. 11 Meso-fabric of soil specimen after the first liquefaction (at 100× magnification)

To further elucidate the influence of *FC* from a meso-fabric perspective, the orientation distribution of particle long axes was analysed for specimens both before and after the first liquefaction. The statistical analysis was performed on 2–3 non-adjacent mesoscopic fields of view at 100× magnification, avoiding the edge regions of the specimen to ensure representativeness. For each *FC*, more than 200 particles were counted. The resulting orientation distributions are presented as rose diagrams in Fig. 12. At the same time, the degree of fabric anisotropy of the sample can be quantified by describing the preferred orientation of the particles (Curray 1956; Riyahikhoo et al. 2025; Pavel et al. 2026), and the expression is as follows:

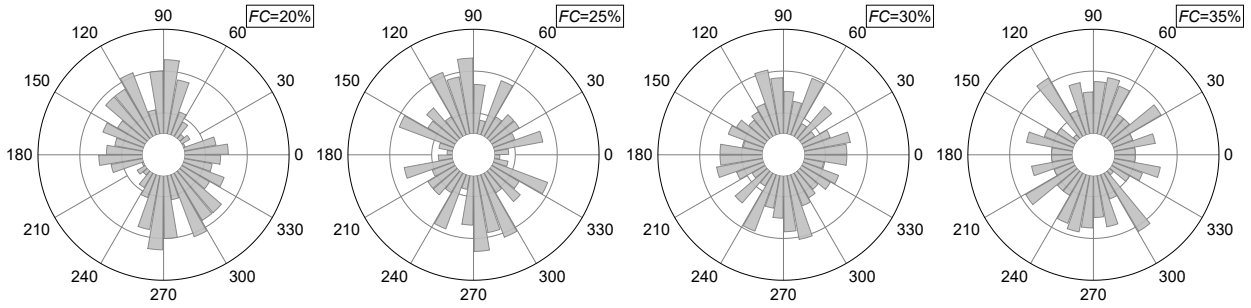
$$I_{ac} = \frac{1}{2\mathrm{N}}\sqrt{\left(\sum_{k=1}^{2\mathrm{N}}\cos 2\theta_k\right)^2 + \left(\sum_{k=1}^{2\mathrm{N}}\sin 2\theta_k\right)^2} \tag{2}$$

Where $2N$ is the total number of particles measured, and θ_k represents the orientation of the long axis of the k_{th} particle relative to the horizontal direction. The value of I_{ac} ranges from 0 to 1, corresponding to perfectly random distribution and ideal horizontal alignment of particles, respectively. Figure 12a shows that for specimens prepared by the moist tamping method with *FC* ranging from 20% to 35%, the long axes were predominantly oriented in the horizontal direction. This contrasted sharply with the isotropic, non-preferential orientation distribution characteristic of clean sand specimens (Ni et al. 2020). This phenomenon may be attributed to the reconfiguration of the soil skeleton by the fine particles. The fines not only filled the pores but also coated the sand grains during moist tamping,

exerting a lubricating effect. This facilitated the rotation of sand grains along the shear direction, allowing them to settle into a stable orientation and thus form a preferred horizontal alignment. These meso-fabric characteristics, when considered alongside the fabric anisotropy evolution during the initial consolidation for different *FC* shown in Fig. 8, provided further explanation for the observed increase in inherent anisotropy of moist-tamped specimen in the sand-like behavior region and its decrease in the silt-like behavior region. In stark contrast, after the first liquefaction, the long axes of particles in all specimens, regardless of *FC*, became predominantly oriented in the vertical direction (Fig. 12b). This indicates that the liquefaction process fundamentally reshaped the meso-fabric, generating a strong fabric anisotropy. However, during the reliquefaction phase, this anisotropic fabric ceased to govern the liquefaction behavior. This is because the coating effect of the fines undermines the orientational stability of the sand skeleton, thereby attenuating the macroscopic manifestation of stress-induced anisotropy and ultimately leading to an elevated reliquefaction resistance.



(a) Specimens prepared by the moist tamping method: I_{ac} = 0.075, 0.064, 0.045, and 0.096



(b) Specimens after the first liquefaction: I_{ac} = 0.066, 0.058, 0.047, and 0.033

Fig. 12 Rose diagrams showing particle orientation distribution of silty sand

4. Conclusions

In this study, a series of undrained cyclic triaxial tests were conducted on sands with eight fines content (*FC* = 0%–35%) to investigate the influence of *FC* on liquefaction/reliquefaction resistance. Based on the volumetric strain observed during consolidation, the evolution of anisotropy was analyzed. Furthermore, an anisotropic coefficient ratio was proposed to characterize the evolution of reliquefaction resistance. The main conclusions are as follows:

(a) Relative value of reliquefaction resistance increased progressively with increasing *FC*. A threshold value of *FC* = 25% was identified, beyond which the reliquefaction resistance surpassed the first liquefaction resistance.

(b) The volumetric-to-axial strain ratio of silty sand exhibits a similar trend under both the initial consolidation

and reconsolidation. The ratio first decreased and then increased with increasing *FC* in sand-like soils, but decreased upon transition to the silt-like soils.

(c) An anisotropic coefficient ratio, R_{ac}, was proposed as an index for evaluating reliquefaction resistance. The reliquefaction resistance of silty sand increased as R_{ac} decreased. For $FC < 25\%$, R_{ac} remained greater than 1.0 and the reliquefaction resistance was lower than the first liquefaction resistance. When $FC \geq 25\%$, R_{ac} decreased below 1.0 and the reliquefaction resistance surpassed the first liquefaction.

(d) Meso-fabric observations showed that fines content changed particle contact mode, pore structure and particle orientation before and after liquefaction. In the silt-like region, fines-coated sand grains weakened interparticle stress transfer, reducing anisotropy's control over the liquefaction process.

Acknowledgements

The work presented in this study was supported by National Natural Science Foundation of China (No. 52578449, No. U2568207), and the science and technology innovation Program of Hunan Province (2024RC4003).

References

Arulanandan K, Sybico J (1992) Post-liquefaction settlement of sand-mechanism and in situ evaluation. Tech Rep NCEER 1(92):239–253

Bao X, Bao Z, Shen J, Chen X, Wu X, Cai H (2024) Dynamic properties of sand with different contents of clay. Powder Technol 431: 119070

Cetin KO, Soylemez B, Guzel H, Cakir E (2025) Soil liquefaction sites following the February 6, 2023, Kahramanmaraş-Türkiye earthquake sequence. Bull Earthq Eng 23(3): 921-944

Cheng K, Zhang J, Miao Y, Ruan B, Peng T (2019) The effect of plastic fines on the shear modulus and damping ratio of silty sands. Bull Eng Geol Environ 78(8):5865-5876

Curray JR (1956) The analysis of two-dimensional orientation data. J Geol 64(2): 117–131

Fardad Amini P, Huang D, Wang G (2021) Dynamic properties of Toyoura sand in reliquefaction tests. Géotech Lett 11(4): 239-246

Fardad Amini P, Wang G (2024) Integrated effects of inherent and induced anisotropy on reliquefaction resistance of Toyoura sand with different strain histories. Géotechnique 74(12): 1276-1290

Finn WDL, Bransby PL, Pickering DJ (1970) Effect of strain history on liquefaction of sand. J Soil Mech Found Div 96(6):1917-1934

Fioravante V, Giretti D, Airoldi S, Moglie J (2021) Effects of seismic input, fine crust and existing structure on liquefaction from centrifuge model tests. Bull Earthq Eng 19(10):3807–3833

Ha IS, Olson SM, Seo MW, Kim MM (2011) Evaluation of reliquefaction resistance using shaking table tests. Soil Dyn Earthq Eng 31(4):682-691

Heng CY, He MC, Qiu YH (2001) Experimental study of liquefaction-resistant characteristics of clayey sand. J Eng Geol 9(4): 339-344

Holzer T, Jayko AS, Hauksson E, Fletcher JPB, Noce TE, Bennett MJ, Dietel CM, Hudnut KW (2010) Liquefaction caused by the 2009 Olancha, California (USA), M5.2 earthquake. Eng Geol 116(1): 184-188

Huang K, Yuan Y (2026) Dynamic centrifuge test on the reliquefaction characteristics of saturated sand deposits subjected to multiple earthquakes. Soil Dyn Earthq Eng 203: 110112

Hussain M, Sachan A (2020) Post-liquefaction reconsolidation and undrained cyclic behaviour of chang dam soil. Adv Comput Methods Geomech: IACMAG Symposium 2019 Volume 1. 77-90

Ishihara K, Okada S (1978) Effects of stress history on cyclic behavior of sand. Soils Found 18(4):31-45

Koester JP (1994) The influence of fines type and content on cyclic strength. In: Prakash S, Dakoulas P (eds) Ground Failures Under Seismic Conditions. Geotechnical Special Publication No. 44. ASCE, Reston, pp 17–33

Lees JJ, Ballagh RH, Orense RP, Van Ballegooy S (2015) CPT-based analysis of liquefaction and re-liquefaction following the Canterbury earthquake sequence. Soil Dyn Earthq Eng 79: 304-314

Lipiński MJ, Wdowska MK, Jaroń Ł (2017) Influence of fines content on consolidation and compressibility characteristics of granular materials. IOP Conf Ser: Mater Sci Eng 245(3): 032062

Liu HL, Zeng CN, Zhou YD (2007) Test study on post-liquefaction deformation behavior of silt ground. Yantu Lixue (Rock and Soil Mechanics) 28(9): 1866-1870

Manzanal D, Bertelli S, Lopez-Querol S, Rossetto Y, Mira P (2021) Influence of fines content on liquefaction from a critical state framework: the Christchurch earthquake case study. Bull Eng Geol Environ 80(6):4871–4889

Mekkiyah HM, Al-Khazragie A (2015) Behavior of clay soil mixed with fine sand during consolidation. Appl Res J 1(8):437-443

Minarelli L, Amoroso S, Civico R, De Martini PM, Lugli S, Martelli L, Molisso F, Rollins KM, Salocchi A, Stefani M, Cultrera G, Milana G, Fontana D (2022) Liquefied sites of the 2012 Emilia earthquake: a comprehensive database of the geological and geotechnical features (Quaternary alluvial Po plain, Italy). Bull Earthq Eng 20:3659-3697.

Monkul MM, Tütüncü YE (2024) Revisiting the effect of relative density on cyclic liquefaction of clean and silty sands: the crossing effect. Bull Earthq Eng 22(8):3817-3843

Ni X, Ye B, Zhang F, Feng X (2020) Influence of specimen preparation on the liquefaction behaviors of sand and its mesoscopic explanation. J Geotech Geoenviron Eng 147(2):04020161

Ni X, Zhang Z, Ye B, Zhang S (2022a) Influence of anisotropy on liquefaction/reliquefaction resistance of granular materials and its quantitative evaluation. Soil Dyn Earthq Eng 161: 107415

Ni X, Ye B, Zhang Z, Zhang S, Zhang F (2022b) An investigation of the influence of reconsolidation properties on the reliquefaction resistance of sand by element tests. J Geotech Geoenviron Eng 148(3): 04021191

Oda M, Kawamoto K, Suzuki K, Fujimori H, Sato M (2001) Microstructural interpretation on reliquefaction of saturated granular soils under cyclic loading. J Geotech Geoenviron Eng 127(5):416-423

Pavel MSH, Toyota H, Takada S, Le NB (2026) Evaluating liquefaction resistance and initial shear modulus considering particle orientation of sand. Soil Dyn and Earthq Eng 201: 109921

Riyahikhoo A, Akhtarpour A, Salari M (2025) Experimental investigation of stress-induced anisotropy on the yield surface of mine tailings. Transp Infrastruct Geotechnol 12(1): 64

Seed HB, Idriss IM, Arango I (1983) Evaluation of liquefaction potential using field performance data. J Geotech Geoenviron Eng ASCE 109(3): 458-482

Shivaprakash BG, Dinesh SV (2017) Dynamic properties of sand–fines mixtures. Geotech Geol Eng 35(5): 2327-2337

Sims JD, Garvin CD (1995) Recurrent liquefaction induced by the 1989 Loma Prieta earthquake and 1990 and 1991 aftershocks: implications for paleoseismicity studies. Bull Seismol Soc Am 85(1): 51-65

Sukhumkitcharoen R, Koseki J, Otsubo M (2024) Relationship between void characteristics and re-liquefaction resistance: An image analysis study. Soils Found 64(6): 101506

Thevanayagam S, Martin GR, Shenthan T, Liang J (2001) Post-liquefaction pore pressure dissipation and densification in silty soils. In: Proceeding of the 4th International Conference on Recent Advances in Geotechnical Earthquake Engineering and Soil Dynamics, San Diego, California, No. 23

Tsukamoto Y, Ishihara K (2022) Evaluating Post-liquefaction Settlement and Lateral Deformation. Adv Soil Liq Eng 115-169

Van Ballegooy S, Malan P, Lacrosse V, Jacka ME, Cubrinovski M, Bray JD, O'Rourke TD, Crawford SA, Cowan H (2014). Assessment of liquefaction-induced land damage for residential Christchurch. Earthq Spectra 30(1): 31-55

Wahyudi S, Koseki J, Sato T, Miyashita Y (2013) Effects of pre-shearing history on repeated liquefaction behaviour of sand using stacked-ring shear apparatus. Bulletin of ERS 46: 3-11

Wang B, Zen K, Chen GQ, Zhang YB, Kasama K (2013) Excess pore pressure dissipation and solidification after liquefaction of saturated sand deposit. Soil Dyn Earthq Eng 49: 157-164

Yamada S, Takamori T, Sato K (2010) Effects on reliquefaction resistance produced by changes in anisotropy during liquefaction. Soils Found 50(1): 9-25

Yang S, Huang D (2023) Investigating the influence of inherent soil fabrics on reliquefaction resistance of sands using DEM-

clump simulation. Comput Geotech 164: 105817

Yasuda S, Harada K, Ishikawa K, Kanemaru Y (2012) Characteristics of liquefaction in Tokyo Bay area by the 2011 Great East Japan earthquake. Soils Found 52(5): 793-810

Ye B, Hu H, Bao X, Lu P (2018) Reliquefaction behavior of sand and its mesoscopic mechanism. Soil Dyn Earthq Eng 114: 12-21

Zhang J, Xiao SH, Huang HW, Zhou JK (2020) Calibrating a standard penetration test based method for region-specific liquefaction potential assessment. Bull Eng Geol Environ 79:5185–5204

Zhang S, Zhong Y, Ni X, Zhang F, Ye B, Zhang Z (2025) An investigation of repeated liquefaction resistance of clayey sand by element test. Soil Dyn Earthq Eng 190: 109188